J. Appl. Comput. Mech., 11(2) (2025) 399-415
DOI: 10.22055/jacm.2024.47217.4677

ISSN: 2383-4536
jacm.scu.ac.ir

Shahid Chamran University of Ahvaz

Journal of Applied and Computational Mechanics

Research Paper

# Insights into Phase Transformations during Selective Laser Melting of Ti6Al4V: A Numerical Approach

**Gasser Abdelal[1], Daniel Higgin[2], Chi-Wai Chan[1], Brian Falzon[3]**

[1] School of Mechanical and Aerospace Engineering, Queen's University Belfast, Northern Ireland, UK
[2] THALAS Group, Belfast, Northern Ireland, UK
[3] Western Sydney University, Sydney, Australia

Received June 19 2024; Revised July 09 2024; Accepted for publication August 07 2024.
Corresponding author: G. Abdelal (g.abdelal@qub.ac.uk).


**Abstract.** Selective Laser Melting (SLM) is a transformative additive manufacturing technique that enables the production of complex metallic components with high precision. Understanding the microstructural evolution during the SLM process is crucial for optimising the mechanical properties and performance of the fabricated parts. This study focuses on developing a predictive model for the microstructure evolution of Ti6Al4V alloy during SLM. The model integrates thermal simulations with phase transformation kinetics using the Johnson-Mehl-Avrami-Kolmogorov (JMAK) theory to predict the formation and dissolution of alpha and martensite phases. The thermal history of the SLM process was simulated using Finite Element Analysis (FEA) in Abaqus, which provided the temperature distribution and cooling rates experienced by the material. These thermal profiles were then used to drive the microstructure evolution model, which predicts the phase fractions and grain structures resulting from the SLM process. The model was validated against experimental data, showing good agreement in predicting phase fractions and microstructural features. Our results highlight the significant impact of processing parameters, such as laser power and scanning speed, on the microstructure of Ti6Al4V. Higher laser powers and slower scanning speeds were found to promote the formation of coarser microstructures, while faster cooling rates led to finer grains and higher martensite fractions. This comprehensive modelling approach provides valuable insights into optimising SLM process parameters to achieve desired microstructural characteristics and improve the mechanical performance of Ti6Al4V parts. The developed model is a robust tool for guiding the design and optimisation of SLM processes, reducing the reliance on trial-and-error methods, and enhancing the efficiency and quality of additive manufacturing for critical applications in aerospace, biomedical, and automotive industries.

**Keywords:** Selective Laser Melting, Ti6Al4V, Additive Manufacturing, Microstructure Evolution, Phase Transformation.

## 1. Introduction

Additive Manufacturing (AM) has revolutionised the production of complex and high-strength metallic components, offering unprecedented design freedom and material efficiency. Among various AM techniques, Selective Laser Melting (SLM) stands out due to its ability to fabricate intricate geometries by selectively melting and fusing layers of metal powder using a high-powered laser. This process is particularly advantageous for producing components from titanium alloys, such as Ti6Al4V, widely used in aerospace, biomedical, and automotive industries due to their excellent strength-to-weight ratio and biocompatibility.

However, the SLM process involves rapid heating and cooling cycles, leading to steep thermal gradients and high cooling rates that significantly influence the microstructure and, consequently, the mechanical properties of the fabricated parts. Understanding and predicting the microstructural evolution during SLM is crucial for optimising process parameters and ensuring the desired performance of the final product.

Selective Laser Melting (SLM) is an advanced additive manufacturing (AM) technique that fabricates complex and high-strength metallic components by selectively melting and fusing metal powder layers using a high-powered laser beam. This process is particularly advantageous due to its ability to produce intricate geometries and reduce material waste. The process parameters, such as laser power, scanning speed, and layer thickness, play a crucial role in determining the quality of the final parts [1, 2]. The SLM process involves rapid heating and cooling cycles, leading to steep thermal gradients and high cooling rates. These thermal phenomena are crucial as they directly influence the fabricated parts' microstructural evolution and mechanical properties. The interaction between the laser and the powder bed results in complex heat transfer mechanisms, including conduction, convection, and radiation, with conduction being the dominant mode [3, 4]. Accurate modelling of these thermal processes is essential for predicting melt pool geometry, solidification patterns, and residual stress formation [5].

Finite Element Analysis (FEA) is widely used to simulate the thermal and mechanical behaviour during the SLM process. These

Published online: August 15 2024

models help understand the temperature distribution, melt pool dynamics, and the resulting microstructures. Key computational challenges include the accurate representation of material properties, the interaction of the laser with the powder bed, and the transient nature of the process [6]. Advanced FEA models incorporate temperature-dependent material properties and detailed boundary conditions to improve predictive accuracy [7]. Despite advancements in modeling techniques, several challenges remain in accurately simulating the SLM process. One major challenge is capturing the dynamic behavior of the powder bed during melting and solidification. Typically represented by a Gaussian distribution, the heat source model needs precise calibration to match the actual process conditions [8]. Additionally, the high computational cost associated with simulating the layer-by-layer nature of SLM poses significant challenges, especially for large-scale parts [9, 10].

The rapid cooling rates in SLM lead to unique microstructural features, such as fine grain structures and high dislocation densities. These features contribute to the distinct mechanical properties of SLM parts. For instance, Ti6Al4V, a widely used titanium alloy, exhibits a complex microstructure comprising $\alpha$ and $\beta$ phases. The phase distribution and morphology are influenced by the thermal history and cooling rates experienced during the SLM process [11]. Accurate thermal models are essential for predicting phase transformations and optimising the mechanical properties of the final parts [12]. Experimental validation is critical for ensuring the reliability of microstructure models. This involves comparing simulation results with experimental data, such as melt pool dimensions and thermal histories obtained through in-situ measurements and post-process analyses. Validated models can provide insights into optimising SLM process parameters, thereby improving part quality and reducing the need for extensive experimental trials [13]. Future research should focus on integrating multiscale models that combine simulations at different scales, from macroscopic thermal and mechanical behaviour to microscopic microstructure evolution. Additionally, incorporating machine learning techniques with traditional modelling methods holds promise for enhancing model accuracy and predictive capabilities [14, 15].

In this study, we develop a predictive model for the microstructure evolution of Ti6Al4V during SLM, integrating thermal simulations with phase transformation kinetics. The model employs the Johnson-Mehl-Avrami-Kolmogorov (JMAK) theory to describe the diffusional and non-diffusional transformations that occur during the process. Finite Element Analysis (FEA) in Abaqus is used to simulate the thermal history of the SLM process, providing detailed temperature distributions and cooling rates.

The objectives of this research are to:

1. Develop a comprehensive model that predicts the microstructural evolution in Ti6Al4V during SLM.
2. Validate the model against experimental data, ensuring its accuracy in predicting phase fractions and microstructural features.
3. Investigate the influence of key processing parameters, such as laser power and scanning speed, on the microstructure and mechanical properties of the fabricated parts.

The findings of this study will provide valuable insights into the optimisation of SLM process parameters, enhancing the efficiency and quality of additive manufacturing for critical applications. By reducing the reliance on trial-and-error methods, the developed model aims to advance the understanding and control of microstructural evolution in SLM, contributing to the broader field of additive manufacturing and materials science.

## 2. Microstructure Modelling Methodology

The microstructure of parts fabricated through Selective Laser Melting (SLM) significantly influences their mechanical properties and overall performance. Understanding and predicting the microstructure evolution during the SLM process is crucial for optimising manufacturing parameters and improving part quality. This section outlines developing and implementing a microstructure evolution model for Ti6Al4V alloy during the SLM process.

The microstructure evolution model is based on the Johnson-Mehl-Avrami-Kolmogorov (JMAK) theory, which describes phase transformations' kinetics under diffusional and non-diffusional conditions. The model incorporates the following key elements:

1. **Diffusional Transformations:** Diffusional transformations are critical in understanding the microstructural evolution of Ti6Al4V during the Selective Laser Melting (SLM) process. These transformations involve the movement of atoms over time, leading to the formation of new phases that significantly influence the mechanical properties of the fabricated parts.

   **Johnson-Mehl-Avrami-Kolmogorov (JMAK) Theory**

   The Johnson-Mehl-Avrami-Kolmogorov (JMAK) theory is employed to describe the kinetics of phase transformations under diffusional conditions. This theory is particularly effective in predicting the formation of the alpha phase from the beta matrix during the cooling process. The JMAK theory accounts for nucleation and growth processes, which are temperature-dependent and vary with the thermal history experienced during SLM.
   Under isothermal conditions, the phase transformation can be described using the JMAK equation:

$$X(t) = 1 - e^{(-k\,t_n)} \tag{1}$$

   where $X(t)$ is the transformed fraction at time $t$, $k$ is the reaction rate constant, and $n$ is the Avrami constant. $k$ and $n$ are temperature-dependent values from experimental data using Temperature-Time-Transformation (TTT) diagrams. They control the rate at which transformation occurs from $\beta$ to the $\alpha$ phase. TTT diagrams are obtained experimentally, showing the phase transformations for isothermal heat treatment. This equation is only usable for diffusion-controlled transformation, i.e. nucleation and growth.

   **Non-Isothermal Conditions and Scheil's Additivity Rule**

   In the SLM process, the temperature conditions are rarely isothermal due to the rapid heating and cooling cycles. To model non-isothermal transformations, Scheil's additivity rule is applied. This approach involves breaking down continuous cooling into a series of small, consecutive isothermal steps. The JMAK equation is applied to each step, and the overall phase fraction is obtained by summing the transformations of these incremental steps. The equivalent time $\tau$ accounts for the temperature changes, allowing the calculation of updated $k$ and $n$ values for each step. The modified JMAK formulation using Scheil's additivity rule is expressed as:

$$X(t) = 1 - \exp\left(-\sum_i k(T_i)\Delta t_i^{n(T_i)}\right) \tag{2}$$

   where $T_i$ represents the temperature at each step, and $\Delta t_i$ is the time increment for that step.

**Equilibrium and Initial Phase Fractions**

For alloys like Ti6Al4V, complete transformation from one phase to another is often impractical due to the presence of minor phases or structural constituents that do not participate in the main transformation. Therefore, the equilibrium fraction $X_{eq}$ and the initial fraction $X_0$ must be considered. The JMAK equation is adjusted to account for these factors, ensuring more accurate predictions of the final phase fractions:

$$X(t) = X_0 + (X_{eq} - X_0)\left[1 - \exp(-kt^n)\right] \tag{3}$$

**Integration with Thermal History**

The thermal history of the SLM process, obtained from Finite Element Analysis (FEA) simulations, is crucial for driving the phase transformation kinetics. The temperature distributions and cooling rates provided by FEA are mapped onto the microstructure model, ensuring that the predictions accurately reflect the thermal conditions experienced during SLM.
By integrating the JMAK theory with detailed thermal simulations, the model can predict the formation and dissolution of phases such as alpha and martensite with high accuracy. This comprehensive approach allows for the optimization of SLM process parameters, ultimately improving the mechanical properties and performance of Ti6Al4V parts.

2. **Diffusion-less Transformations:** Martensite formation is modelled using a different approach, considering the rapid cooling rates that bypass diffusional processes. This transformation is typically characterized by the instantaneous conversion of the beta ($\beta$) phase to martensite ($\alpha'$) when the temperature drops below the martensite start temperature ($M_s$). These transformations begin to occur during cooling around the martensitic temperature $M_s$, which is determined empirically. Additionally, some residual martensite phase ($M_0$) may be present and must be accounted for in the model.
The dissolution of martensite ($\alpha_m$) occurs during heating but can also take place during isothermal treatments and even during prolonged cooling at temperatures above the martensite dissolution temperature ($T_{mdiss}$). This behaviour is critical to accurately model the thermal cycles experienced during the Selective Laser Melting (SLM) process.
The Koistinen-Marburger law [16], initially developed for martensitic transformations in steels, has been shown to be effective for other alloys as well, including Ti6Al4V [17]. This empirical law provides a relationship for predicting the volume fraction of martensite ($X_M$) formed as a function of temperature:

$$X_M = M_0\left(1 - e^{\left(-\gamma(T - M_s)\right)}\right) \qquad ,(T < M_s) \tag{4}$$

where $\gamma$ is a constant dependent on the material being investigated.
This approach captures the rapid nature of the martensitic transformation, which is not influenced by diffusion but rather by the shear mechanism that rapidly converts the $\beta$ phase into martensite. The presence of residual martensite ($M_0$) is accounted for, ensuring that the transformation kinetics are accurately represented under various thermal conditions.
Understanding and modelling these diffusion-less transformations are crucial for predicting the final microstructure of Ti6Al4V parts produced by SLM. The ability to accurately predict martensite formation and its subsequent dissolution during thermal cycles allows for better control of mechanical properties, as martensite contributes significantly to the strength and hardness of the material.
By integrating the Koistinen-Marburger law with the thermal history obtained from Finite Element Analysis (FEA), the model ensures precise predictions of martensite formation. This integration is essential for optimizing SLM process parameters, such as laser power and scanning speed, to achieve desired microstructural characteristics and enhance the performance of the fabricated parts.

3. **Phase Transformation Parameters:** JMAK parameters can be inversely calculated from TTT, or CCT diagrams [18]. In order to calculate values for reaction rate $k$ and Avrami constant $n$, two conventional values (i.e. a start $X_s$ and finish $X_f$ volume fraction) are chosen, and the fraction is measured. These values are usually 1/5% or 95/99%. The TTT diagrams extract start and finish times $t_i(T)$ and $t_f(T)$ when the transformation reaches $X_s$ and $X_f$, respectively. Then, the parameters of the JMAK transformations are obtained as:

$$k = \frac{\ln(1 - X_s)}{t_s^n}$$
$$n = \frac{\ln\dfrac{\ln(1 - X_s)}{\ln(1 - X_f)}}{\ln\left(\dfrac{t_s}{t_f}\right)} \tag{5}$$

The JMAK parameters $k_{dis}(T)$ and $n_{dis}(T)$ that define the transformation of $\alpha_{mdis}$ are calculated using TTT curves obtained from the available experimental data of martensite dissolution. These experimental data have to be normalised by dividing the date of dissolved $\alpha_{mdis}(T)$. This allows the use of the $k_{dis}$ and $n_{dis}$ parameters in JMAK equations representing a fully complete evolution of $\alpha_{mdis}$ from 0 (no dissolution) to 1 (complete dissolution $\alpha_{mdis} = \alpha_{mdis}^{eq}$).

The thermal history of the SLM process, obtained from Finite Element Analysis (FEA) simulations, is used as an input to the microstructure model. The temperature distribution and cooling rates provided by the FEA simulations drive the phase transformation kinetics. This integration ensures that the microstructure evolution model accurately reflects the thermal conditions experienced during the SLM process. The microstructure model is implemented using a finite element mesh that discretises the geometry of the SLM part.
The following steps are involved in the implementation:

1. **Temperature Mapping:** The thermal history from the FEA simulations is mapped onto the finite element mesh. This mapping provides the temperature profile for each element in the mesh over time.

The microstructure of Ti6Al4V usually consists of a mixture of two solid phases at room temperature, $\alpha$ and $\beta$. When new layers are added to the part, the previously deposited material undergoes heating/cooling cycles that may induce microstructural and properties changes. The fast heating and cooling near the fusion zone can introduce diffusion-less transformations. It is also essential to consider the diffusion-based transformations between deposited material layers and during heat treatment, often

performed for SLM parts to reduce residual stresses. Four transformations should be considered. Ti6Al4V can undergo two transformations during heating: dissolution of alpha $X_\alpha$ and dissolution of martensite $X_m$. When cooling below the $\beta-$Transus temperature, two transformations can occur: either the formation of alpha $X_\alpha$ or martensite $X_m$ from the beta $\beta$ phase. Above the $\beta$ transus temperature, the structure will consist of the $\beta$ phase. Cooling below this temperature will result in one of two transformations: diffusion-controlled transformation of $\beta \rightarrow \alpha$ or diffusion-less transformation of $\beta \rightarrow \alpha'$, depending on the cooling rate used. During heating, the microstructure will transform depending on the initial phase. If the microstructure formed in the first thermal cycle is composed of $\alpha+\beta$, reheating will lead to diffusion-controlled $\alpha \rightarrow \beta$ transformation. Martensitic decomposition can also occur if the phase is present after the Martensitic temperature is reached. If the decomposition is incomplete, tempering results in a three-phase microstructure of $\alpha_m+\alpha+\beta$.

2. **Phase Fraction Calculation:** For each time step, the phase fractions of alpha, beta, and martensite are calculated based on the local temperature and the transformation kinetics described by the JMAK theory and the martensitic transformation model.

The formation of $\alpha$ can then be determined from the previous $\alpha$ and $\beta$ fractions $\alpha_0$ and $\beta_0$, the equilibrium $\alpha$ fractions $\alpha_{eq}$ and JMAK parameters $K_\alpha$ and $n_\alpha$ determined from TTT diagrams:

$$\begin{aligned} \alpha(T) &= \left(1-\exp^{-K_\alpha(\tau_\alpha)n_\alpha}\right)\left(\alpha_{eq}\right)\left(\alpha_0+\beta_0\right) \\ \tau_\alpha &= \left(-\ln\left(1-\frac{\alpha_0 \diagup \alpha_{eq}}{\beta_0+\alpha_0}\right)/K_\alpha\right)^{\frac{1}{n_\alpha}} \end{aligned} \tag{6}$$

For high cooling rates, above 410°/S, the $\beta$ phase may undergo diffusion-less transformation to a martensitic phase when cooling below the martensite start temperature $M_s$ ~ 650–500°C. For a cooling rate slower than 410 C/s and above 20 C/s, the total transformation of $\beta$ to $\alpha_m$ is impossible, and a partial transformation will occur. This microstructure resulting from this transformation has been classified as massive martensite. No distinction has been made in this model to reduce complexity. This approach has been used in many research works [19, 20] as the transformations have a similar composition and mechanical behaviour. As in the alpha formation, some $\beta$ may be retained depending on the Vanadium content. It has been shown by Reference that the $\beta$ phase may be retained if the starting volume fraction of the alloy is less than 0.25. This transformation of $\beta \rightarrow \alpha_m$ is described by the Koistinen & Marburger [17] equation given below:

$$\begin{aligned} \alpha_m(T) &= \left(1-\exp\left(-\gamma\left(M_s-T\right)\right)\left(\beta_0+\alpha_{m0}\right)\right), \quad \Delta T > 410\ C/s \\ \alpha_m(T) &= \left(1-\exp\left(-\gamma\left(M_s-T\right)\right)\left(\beta_0+\alpha_{m0}-\alpha_{eq}\right)\right), \quad 20\ C/s < \Delta T < 410\ C/s \end{aligned} \tag{7}$$

where $\alpha_{m0}$ is the volume fraction of the martensite phase available at the beginning of the reaction, and $\gamma$ is the Koistinen & Marburger constant.

The diffusional dissolution of $\alpha$ (or reformation of $\beta$) occurs when heating processes above $\beta$ transus temperature and the $\beta$ phase fraction is lower than that of the $\beta$ equilibrium fraction $\beta_{eq}$. Kelly's empirical model [21] has been employed to deal with such transformation. The model depends on a temperature-dependent function $F_{diss}(T)$ described by:

$$F_{diss}(T) = 2.2\times10^{-31}\ T^{9.89} \tag{8}$$

with the $\alpha$ dissolution being:

$$\begin{aligned} \alpha(T) &= 1-\left(1-\alpha^{eq}\right)F_{diss}\sqrt{\left(\Delta t+\tau_{diss}\right)}, \quad 0<\Delta t+\tau_{diss}<t_{crit} \\ \alpha(T) &= \alpha^{eq}, \quad \Delta t+\tau_{diss}>t_{crit} \end{aligned} \tag{9}$$

where $t_{crit}$ is the time for the reaction to be complete and where $\tau_{diss}$ is the relative time needed to reach the phase fraction $\beta_0$ with the new evolution law dependent from $F_{diss}(T)$:

$$\tau_{diss} = \left(\frac{\beta_0}{F_{diss}(T)\left(1-\alpha^{eq}\right)}\right) \tag{10}$$

At room temperature, $\alpha_m$ is stable. If the alloy is heated higher than the martensitic dissolution, start temperature ($m_{diss}$) ~ 400°C, and the martensitic fraction is more significant than the equilibrium value, the martensite phase will transform to $\alpha$ and $\beta$. $m_{diss}$ is temperature-dependent and will increase towards 1 with an increase in temperature to the $\beta$ phase start temperature. If the decomposition is incomplete, tempering results in a three-phase microstructure of $\alpha_m+\alpha+\beta$. This transformation can also happen for isothermal treatment. The $\alpha$ structure formed has a different composition to Widmanstatten alpha; however, this difference is ignored to reduce complexity.

The transformation is diffusion-controlled, and the JMAK equation also describes its kinetics. To use the JMAK equations, a temperature-dependent function of maximum dissolvable martensite at equilibrium $\alpha^{eq}_{mdis}(T)$ is defined from the experimental data. The fraction $\alpha_{mdis}$ at the equivalent time $\tau_m$ at temperature $T$ is computed as:

$$\begin{aligned} \alpha_m(T) &= \left(1-\exp^{-k_m(\tau_m)n_m}\right) \\ \tau_m &= \left(-\ln\left(1-\frac{\alpha_{m0}-\alpha_{meq}}{\beta_0+\alpha_{m0}-\alpha_{meq}}\right)/k_m\right)^{\frac{1}{n_m}} \end{aligned} \tag{11}$$

where $k_m$ and $n_m$ are the JMAK parameters determined from phase transformation diagrams. Sun [20] developed equations to calculate these values below:

$$k_m(T)=\begin{Bmatrix}-4.58\times10^{-5}\,T+1.04, & T<793\ K\\ 5.4\times10^{-5}\,T+0.74, & T\geq793\ K\end{Bmatrix} \tag{12}$$

$$n_m(T)=\begin{Bmatrix}-4.39\times10^{-3}\,T+1.09, & T<793\ K\\ 7.33\times10^{-4}\,T+0.74, & T\geq793\ K\end{Bmatrix} \tag{13}$$

The martensite equilibrium $\alpha_{meq}$ value can be determined experimentally and represented by the equation below. $T_A$ is a constant taken as 723 K obtained from thermodynamic data:

$$\alpha_{meq}(T)=0.5\left(1+\tanh\left(\frac{T_A-T}{80}\right)\right) \tag{14}$$

Abaqus FE solver was used to calculate the thermal evolution during the process, and state-dependent variables were used to record the individual phase fractions. The heat equation governs the spatial and temporal distribution of the temperature:

$$\rho C\frac{\partial T}{\partial t}=\nabla\bullet(k\nabla T)+Q \tag{15}$$

where $\rho$ is the density, $C$ is the specific heat capacity, $k$ is the thermal conductivity, $T$ is the temperature, $t$ is the time, and $Q$ is the absorbed heat.

During SLM, the heat generated from the laser beam is absorbed and reflected by the metal powders. User subroutine DFLUX was used to model the laser input as a moving heat flux with a Gaussian distribution on top of the powder bed surface. Equation [16] shows the expression used to find the input heat flux q:

$$q=\frac{2AP}{\pi ab}\exp\left(-3\left(\left(\frac{x}{a}\right)^2+\left(\frac{y-v_st}{b}\right)^2\right)\right) \tag{16}$$

where $A$ is the absorption coefficient, $P$ is the laser power, $R$ is the effective laser beam radius, $v$ is the laser beam velocity, $x$, $y$ are the grid node coordinates and $x_0$, $y_0$ are the coordinates of the start focus point. The value of 0.3 was taken for the laser absorptance [17] and assumed constant throughout the simulation.

The initial temperature distribution in the substrate or powder beds can be expressed in Eq. (3). In addition to the environment temperature being controlled, the bottom surface of the substrate is often set to a controlled temperature. Therefore, a fixed thermal boundary condition at the substrate can be applied in the model as shown in Eq. (4):

$$T(x,y,z,0)=T_\infty \tag{17}$$

$$T(x,y,0,t)=T_s \tag{18}$$

where (x, y, z) is the position, $T_\infty$ is the ambient temperature, and $T_s$ is the preheat temperature. Conditions were set at the beginning of the simulation to ensure accurate results. The ambient temperature is uniform and was assumed to be room temperature and was set as $T_\infty$ = 293 K. In comparison, the substrate temperature is set to $T_s$ = 373 K when applied.

The laser beam energy is absorbed on the powder layer surface. Most energy is conducted into nearby powder particles through the melt pool or the build platform. In contrast, some energy is lost to convection and radiation from the surface. Therefore, conductive heat losses have been applied using a surface film condition. As only a small area has been modelled, this condition has been applied to the side surfaces to simulate losses to surrounding powder and to the bottom surface to simulate conductive heat loss to the substrate.

The surface of the powder bed experiences convection and radiation. Both radiation and convection can add to the non-linearity of analysis as they are temperature-dependent, increasing computational costs. Therefore, convection and radiation conditions have been applied to the top surfaces and modelled as a combined boundary equation to reduce computational costs. The equation below has been implemented with user-subroutine FILM to model convection and radiation:

$$h=h_c+\varepsilon_p\sigma\left(T^2+T_0^2\right)\left(T+T_\infty\cong2.41\times10^{-3}\varepsilon_pT^{1.61}\right) \tag{19}$$

where $\varepsilon_p$ is the powder emissivity. A constant value for emissivity and convection coefficient has been chosen. In this case, 0.3 and 10 W/m$^2$K have been used, respectively. Fluidity has been ignored due to the small melt pool sizes that will be modelled. The bottom of the powder layer has been assumed to be in complete contact with the substrate below and has perfect thermal contact. The temperature-dependent thermophysical properties of SS316L used in the model are listed in Table 1 and were obtained from published literature by Mills [17].

The proposed model was used to predict the metallurgical phase evolution for SLM. A thin wall measuring 3 x 0.2 x 1 mm (L-W-H) 5.6. A stainless steel substrate measuring 5 mm in height was used as a base, while previous melted layers of Ti6Al4V were considered to be melted on the substrate. Boundary conditions were set for the substrate, and pre-melted layers with an initial temperature of 20°C and convection and radiation were applied. Five layers of 60 μm thickness were deposited onto the sample after a re-coating time of 0.5 seconds. Abaqus's "Model Change" interaction activated the required layer where a heat flux load was applied, and radiation and boundary conditions were set. A 25 x 25 x 10 μm mesh was used for the power layers, while a coarser mesh of 50 x 25 μm was used for the substrate and previously melted layers. The coarser mesh height increased from 10 μm to 90 μm as the distance from the melt zone increased.

Each scan melts and rapidly solidifies as it passes over a powder layer. Figure 2 shows the temperature contour at the end of the fifth. The laser beam's heat energy can penetrate multiple layers and leave a comet-shaped tail behind. The temperature evolution is analysed in Fig. 3. It shows the thermal cycles obtained from the FEM at the central node on the top surface for layers 1 to 5. As the laser passes over a node, temperature increases sharply above the melting point marked in the figure. The temperature then rapidly drops back down, solidifying.

**Table 1.** Ti6Al4V solid alloy thermo-physical properties with increasing temperatures.

| Temperature (K) | Density (kg/m³) | Specific Heat (J/kg·K) | Conductivity (W/m·K) |
|---|---|---|---|
| 298.0 | 4420.0 | 546.0 | 7.0 |
| 373.0 | 4406.0 | 562.0 | 7.45 |
| 473.0 | 4395.0 | 584.0 | 8.75 |
| 573.0 | 4381.0 | 606.0 | 10.15 |
| 673.0 | 4366.0 | 629.0 | 11.35 |
| 773.0 | 4350.0 | 651.0 | 12.6 |
| 873.0 | 4336.0 | 673.0 | 14.2 |
| 973.0 | 4324.0 | 694.0 | 15.5 |
| 1073.0 | 4309.0 | 714.0 | 17.8 |
| 1173.0 | 4294.0 | 734.0 | 20.2 |
| 1268.0 | 4282.0 | 753.0 | 22.9 |
| 1268.0 | 4282.0 | 693.0 | 19.3 |
| 1373.0 | 4267.0 | 660.0 | 21.9 |
| 1473.0 | 4252.0 | 678.0 | 23.8 |
| 1573.0 | 4240.0 | 696.0 | 25.6 |
| 1673.0 | 4225.0 | 714.0 | 24.6 |
| 1773.0 | 4205.0 | 732.0 | 23.4 |
| 1873.0 | 4198.0 | 750.0 | 27.0 |
| 1923.0 | 4189.0 | 759.0 | 28.0 |
| 1923.0 | 3920.0 | 1007.0 | 83.5 |
| 1973.0 | 3886.0 | 831.0 | 83.5 |
| 2073.0 | 3818.0 | 831.0 | 83.5 |
| 2173.0 | 3750.0 | 831.0 | 83.5 |

The thermal gradient is substantial around the spot of the laser but decreases as time progresses. During the re-coat phase, the material cools down until a second laser pass is applied above, where there is a sharp increase in temperature once again. Taking layer one as an example: the energy from the laser on the second layer is enough to cause remelting. With each subsequent layer, the reheat temperature reduces, rising above the $\beta$ transus temperature in the third scan and the martensite start temperature in the fourth scan. The difference in maximum temperatures at each layer is due to the residual heat from the previous layers. Additionally, the laser beam scan point does not pass directly over the chosen node in each layer.

Within the model, several assumptions have been made that add to the uncertainty in its ability to predict the microstructure evolution correctly. As Ti6Al4V is still being researched and models developed, there are varying temperature points and kinetic parameters. This thesis has tried to use the most commonly used values found in the literature or a median value if the range of values was extensive. Gathering the JMAK parameters can also be another source of uncertainty, as experimental characterisation can be pretty noisy. $\alpha$ phases may be mischaracterised as morphology is similar between phases. For example, the Widmanstatten $\alpha$ and martensitic $\alpha$ have a dendritic form that may be misinterpreted. High temperatures involved are also difficult to calibrate and measure in situ. This is one of the reasons there is a lack of experimental data available to validate, along with the time and cost needed to record phase evolution with temperature and time. The parameter discrepancy indicates that further research is required and why Ti6Al4V microstructure evolution is still a topic of discussion. In addition, the JMAK equation is very sensitive to its inputs, where small changes to a single parameter can result in significant differences in phase fractions.

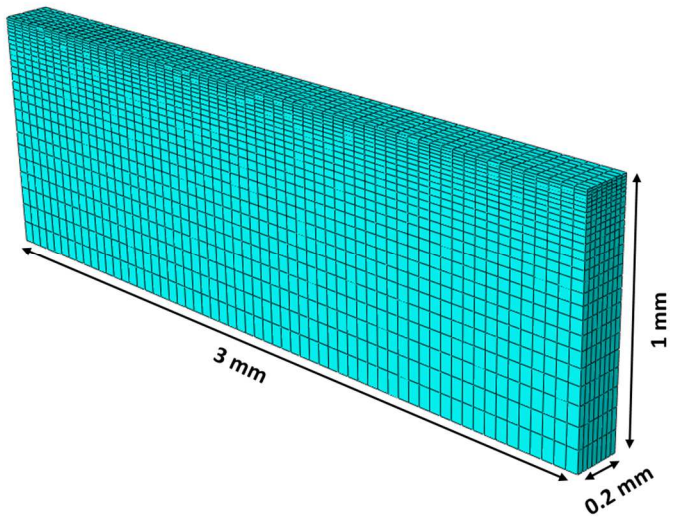


**Fig. 1.** Finite Element Mesh for thin-walled sample.

Similar to validating the thermal model, the range of processing parameters can make it hard to validate models quantifiably. Different geometries/scan patterns also need to be investigated as they will have different thermal histories during the process and thus have different microstructures. As in the thermal model, thermal gradients are high, requiring a fine mesh and small-time incrementation to allow convergence requiring significant computational power/time. As many of the JMAK parameters are temperature dependent, an incorrect thermal history can lead to more variables being used. This is why the thermal model was developed and validated against multiple sources, so the generated data may be used as an input for the phenomenological model.

## 3. Verification of SLM Model

Verifying the Selective Laser Melting (SLM) model is critical to ensure its accuracy and reliability in predicting phase transformations and microstructural evolution. This section outlines the comprehensive validation process using experimental data from the literature and in-house experiments. The model's predictions are compared with experimental results obtained through resistivity measurements and Differential Scanning Calorimetry (DSC) techniques.

The model's validation process begins with a comparison to alpha fraction measurements by Malinov using DSC. This method provides detailed insights into the kinetics of the beta $(\beta)$ to alpha $(\alpha)$ phase transformation under various cooling rates. The DSC data and resistivity measurements offer a robust dataset for validating the model's ability to predict the phase fractions accurately. These initial comparisons show good agreement, particularly in predicting alpha and martensite fractions under different cooling rates.

The model is further tested using data from Directed Energy Deposition (DED) experiments conducted by Babu et al. [25]. These experiments involve repeated thermal cycling and provide a different thermal history than SLM, offering a rigorous test of the model's versatility. The thermal data from these experiments, characterised by cyclic heating and cooling rates, validate the model's predictions of phase transformations, particularly the formation of alpha, beta, and martensite phases.

The validation process demonstrates the model's robustness and accuracy across different additive manufacturing techniques by comparing the model's predictions with experimental results from both DSC and DED studies. This multi-faceted approach ensures that the model can reliably predict phase transformations under various thermal conditions, enhancing its applicability for optimising SLM process parameters and improving the mechanical properties of fabricated parts.

The model is validated using experimental data from literature and in-house experiments. Techniques such as resistivity measurements and Differential Scanning Calorimetry (DSC) are employed to compare the predicted phase fractions with experimental results. The validation shows good agreement, particularly in predicting the alpha and martensite fractions under different cooling rates. Initially, the model's predictions are compared with alpha fraction measurements by Malinov using DSC [23] and resistivity [24]. Subsequently, the model is applied to a Directed Energy Deposition (DED) problem using experimental data from Babu et al. [25], providing a comprehensive validation across different additive manufacturing techniques.

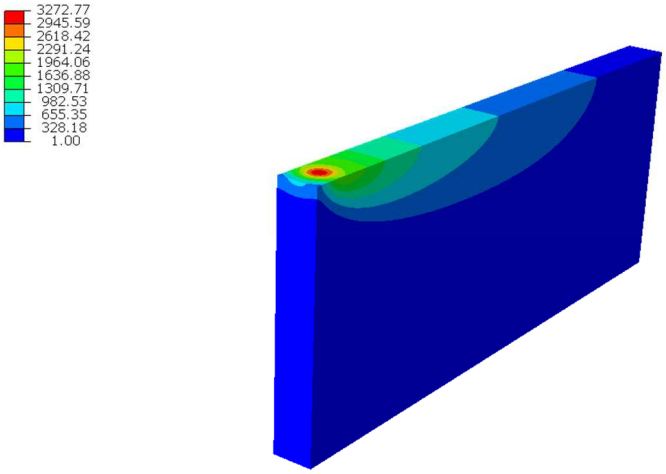


**Fig. 2.** Three-dimensional temperature field at end of fifth laser scan of SLM process.

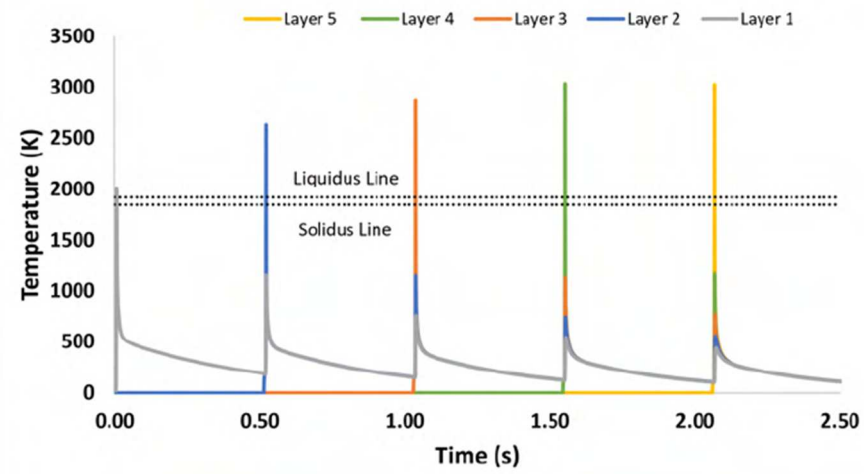


**Fig. 3.** Temperature evolution at end of each of the five layers. Measured from the centre of each layer.

### 3.1. Resistivity and DSC Measurements – Malinov

The section "3.1 Resistivity and DSC Measurements – Malinov" details the validation of the developed model against experimental data obtained through resistivity measurements and Differential Scanning Calorimetry (DSC). This validation is crucial for ensuring the model accurately predicts the phase transformations occurring during the Selective Laser Melting (SLM) process of Ti6Al4V.

**Experimental Setup and Thermal History**

The initial work referenced by Malinov involves using DSC to study the kinetics of the beta ($\beta$) to alpha ($\alpha$) phase transformation under different cooling rates. In Malinov's experiments, Ti6Al4V samples were heated beyond the beta transus temperature to ensure a 100% $\beta$ phase. Subsequently, these samples were cooled at varying rates, ranging from 5 to 50°C per second. Malinov developed continuous-cooling transformation (CCT) diagrams and derived the Johnson-Mehl-Avrami-Kolmogorov (JMAK) parameters, enabling the modelling of the $\beta$ to $\alpha$ transformation for various cooling paths and conditions.

**Model Implementation and Initial Conditions**

Malinov's experiments observed some martensite formation at the highest cooling rates. However, the simulation in this study considered only the $\beta$ to $\alpha$ transformation, setting the martensite fraction to zero. This simplification was necessary because the primary focus of the experimental data was on the $\beta$ to $\alpha$ transformation. Figure 4 in this paper compares the experimental measurements of the α phase over time for different cooling rates with the simulated $\alpha$ fractions.

The model tends to over-predict phase transformation early and lacks the characteristic S-shaped curve observed in Malinov's experimental data. This discrepancy is most pronounced at faster cooling rates. Different cooling rates lead to varying growth rates of phases, requiring adjustments in the JMAK parameters. Although the model attempts to account for temperature-dependent JMAK parameters, further refinements are necessary to index these parameters for different heat treatments accurately. Additionally, the absence of martensite fraction measurements in Malinov's work may contribute to differences between the experimental and simulated results.

**Comparative Analysis and Validation**

To further validate the model, it was compared against resistivity measurements conducted by Malinov during isothermal heating of Ti6Al4V. This comparison showed good agreement between the measured isothermal $\alpha$ fractions and the model's predictions. Figure 5 shows the comparison, indicating that while more significant discrepancies appear at the beginning of the simulation for higher isothermal exposure temperatures, the predictions balance out over time. This suggests the model can reliably predict phase transformations during isothermal conditions, enhancing its applicability to various thermal histories encountered in SLM.

The validation through resistivity and DSC measurements underscores the robustness of the developed model. This section provides a crucial step in verifying the model's accuracy by aligning the predictions with established experimental data. This validation process bolsters confidence in the model's predictions and highlights areas for further refinement, such as improving the accuracy of temperature-dependent JMAK parameters and accounting for martensite formation under certain conditions.

**Key Insights and Implications**

The successful validation of the model against resistivity and DSC measurements highlights several key insights:

1. **Model Accuracy**: The model's ability to closely match experimental data under various cooling rates and isothermal conditions underscores its accuracy and reliability in predicting phase transformations.
2. **Temperature-Dependent Parameters**: The need for accurate temperature-dependent JMAK parameters is evident, as discrepancies in these values can lead to significant differences in predicted phase fractions.
3. **Martensite Formation**: The absence of martensite measurements in the validation experiments points to an area for further investigation. Incorporating these measurements could improve the model's predictive capability.

The comprehensive validation of the model against experimental data from DSC and resistivity measurements demonstrates its accuracy and applicability in predicting phase transformations during the additive manufacturing of Ti6Al4V. The insights gained from these validations guide further refinements, ensuring more precise predictions of microstructural evolution. Ultimately, this enhances the optimisation of additive manufacturing process parameters for critical aerospace, biomedical, and automotive applications.

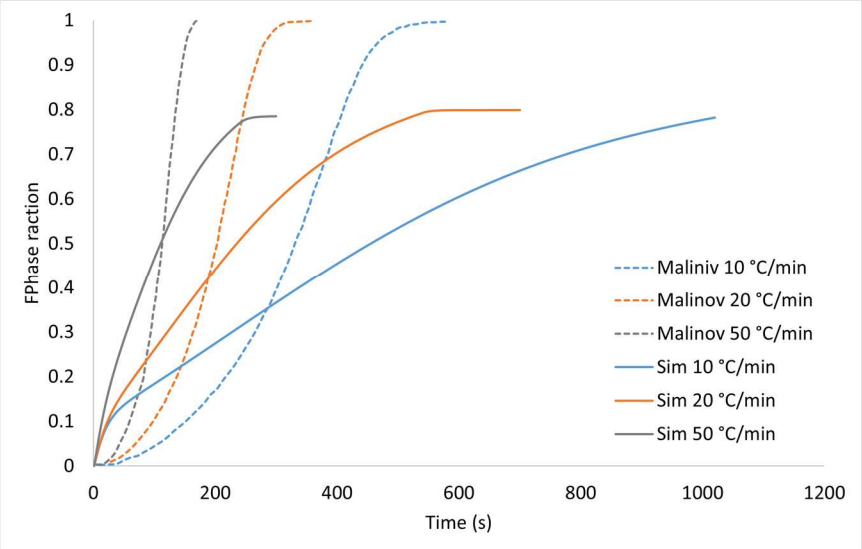


**Fig. 4.** Alpha Phase Fraction for continuous cooling rates compared with Malinov [23].

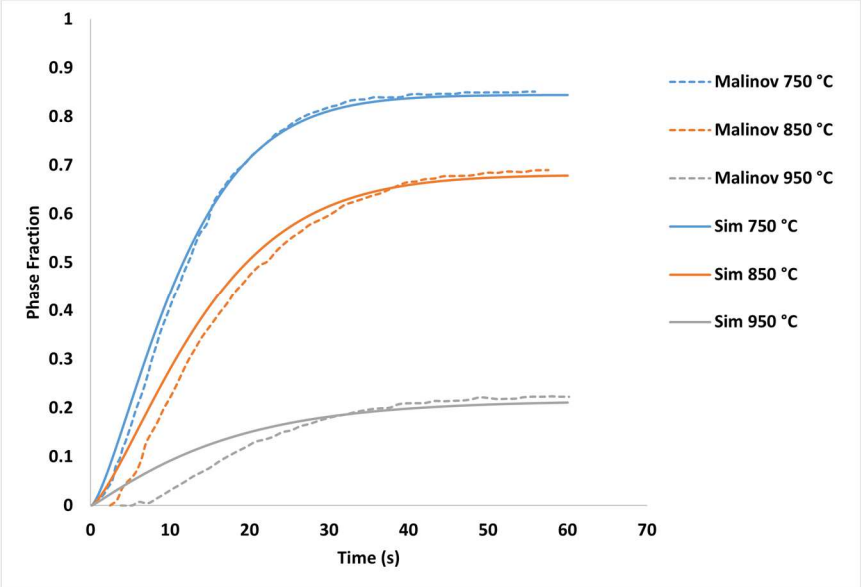


**Fig. 5.** Alpha Phase Fraction for isothermal conditions compared with Malinov [23].

### 3.2. Direct Energy Deposition -Babu-Kelly

Following the validation against resistivity and DSC measurements, Section 3.2 extends the application of the developed model to Direct Energy Deposition (DED) processes. This section leverages data from the work of Babu et al. [25], providing a critical test of the model's capability to predict phase transformations under the distinct thermal histories and cooling rates characteristic of DED processes.

**Experimental Setup and Thermal History**

In the study by Babu et al. [25], the phase transformation kinetics during repeated thermal cycling of Ti6Al4V were meticulously examined using time-resolved X-ray diffraction. Laser metal deposition induced cyclic heating and cooling rates up to 20°C/s, simulating the conditions typically encountered in DED. The recorded thermal history from these experiments, which featured peak temperatures between 1100°C and 600°C, served as a basis for validating the model's predictions.

**Model Implementation and Initial Conditions**

The predictive model calculated phase fractions over time, focusing on the transformation from $\alpha$ to $\beta$ phases and the subsequent formation of martensite during cooling. Initial phase fractions were set at 0.91 for α and 0.09 for $\beta$, reflecting the starting composition. As thermal energy was introduced, the $\alpha$ phase transformed into $\beta$, and at temperatures exceeding the $\beta$ transus line, the material transitioned entirely to the $\beta$ phase. Notably, martensite formation was observed immediately after thermal loading, particularly following the first and second thermal cycles, indicating rapid cooling effects.

**Comparative Analysis and Validation**

Figures 6, 7 and 8 compare the model's predictions and the experimental data. Figure 6 illustrates the thermal history and the total $\alpha$ phase fraction extracted from Babu's experiments. Figure 7 depicts the dynamic evolution of phase fractions throughout the thermal cycles, including total $\alpha$, $\beta$, and martensite phases. Finally, Fig. 8 offers a comparative analysis of the phase fractions calculated by the current model, those predicted by Murgau, and the empirical data provided by Babu et al. [25].

The validation results demonstrated a strong correlation between the model's predictions and the experimental observations, particularly concerning the total $\alpha$ phase fraction and martensite formation during cyclic thermal loading. This agreement underscores the model's accuracy and robustness, validating its applicability across different additive manufacturing techniques beyond SLM.

**Key Insights and Implications**

The successful application of the model to DED processes highlights several key insights:

1. **Versatility of the Model:** The model's ability to accurately predict phase transformations in SLM and DED processes underscores its versatility and robustness. This adaptability is crucial for optimising additive manufacturing processes across different applications and materials.
2. **Impact of Thermal Cycles:** The detailed analysis of thermal cycles and their effect on phase transformations provides valuable insights into optimising process parameters for DED. Understanding the interplay between heating and cooling rates is essential for controlling microstructural evolution and, consequently, the mechanical properties of the fabricated parts.
3. **Guidance for Process Optimisation:** The validated model is a powerful tool for optimising DED process parameters. By accurately predicting phase transformations, the model can help fine-tune laser power, scanning speed, and other critical parameters to achieve the desired microstructural characteristics.

The comprehensive validation of the model against experimental data from DSC, resistivity measurements, and Direct Energy Deposition experiments demonstrates its accuracy and applicability in predicting phase transformations during the additive manufacturing of Ti6Al4V. The insights gained from these validations guide further refinements, ensuring more precise predictions of microstructural evolution. Ultimately, this enhances the optimisation of additive manufacturing process parameters for critical aerospace, biomedical, and automotive applications.

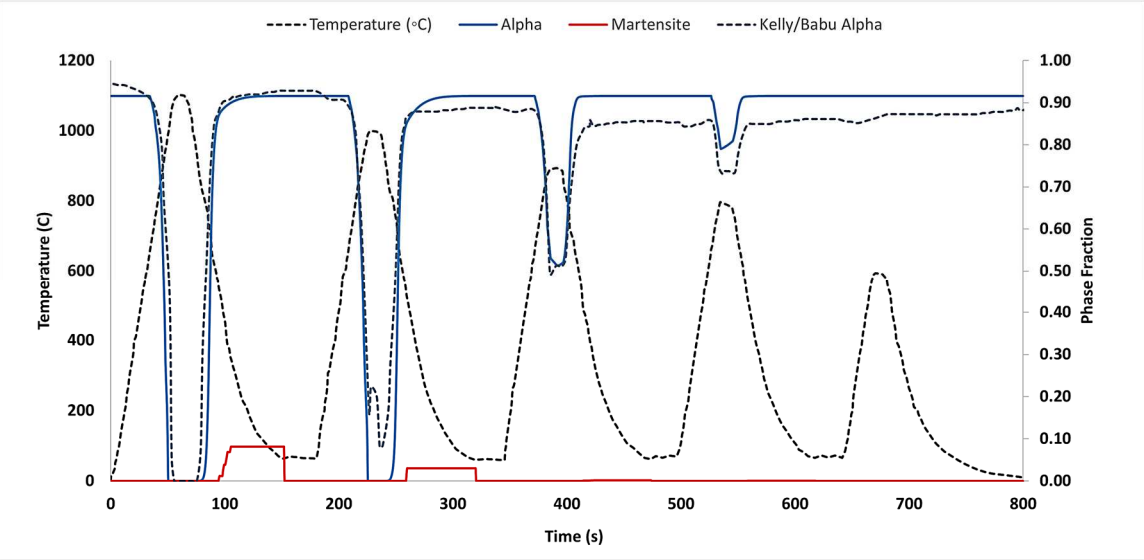


**Fig. 6.** Thermal history and total $\alpha$ phase fraction extracted from Babu et al. [25].

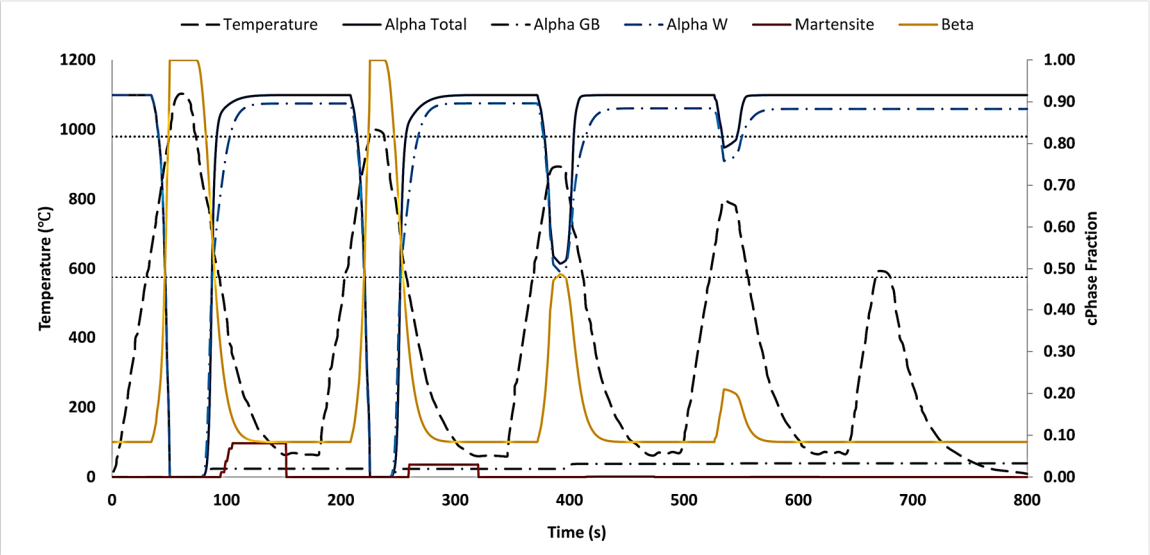


**Fig. 7.** Phase evolution of total alpha, beta, martensite, alpha grain boundary and alpha Widmanstatten. Thermal history is plotted along with beta transus and martensite start temperatures.

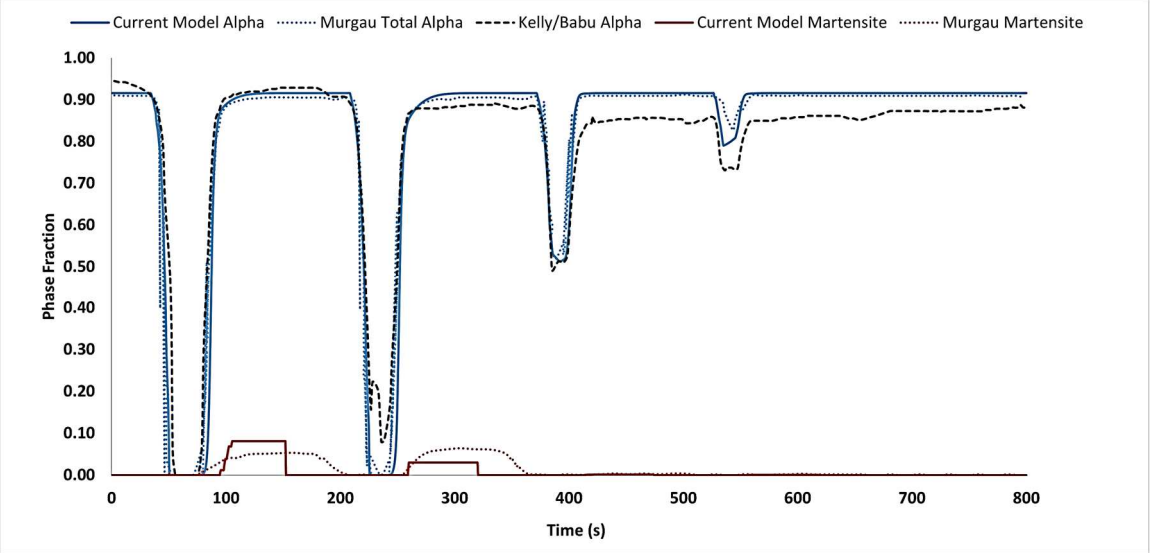


**Fig. 8.** Total calculated alpha and martensite fraction with current model compared with Babu et al. [25] and Murgau [26].

**Table 2.** Processing parameters used in microstructure simulations.

| | Case 1 | Case 2 | Case 3 |
|---|---|---|---|
| Power (W) | 100 | 200 | 100 |
| Velocity (mm/s) | 200 | 200 | 400 |
| Beam Radius (mm) | 0.1 | 0.1 | 0.1 |

## 4. SLM Application

This section will apply the microstructure model for an SLM application where five scans on five layers of Ti6Al4V are modelled. As each layer is deposited the initial phase fractions are set as 0.9 $\alpha$, 0.1 $\beta$ and 0.0 martensite. Three cases were considered. The first case modelled typical SLM processing parameters. Two other cases were considered to investigate the influence of processing parameters on the microstructure evolution. In the second case, the power was adjusted from 100 to 200W, while in the third, the scanning velocity was changed from 200 mm/s to 400 mm/s.

The processing parameters used during the simulations are reported in Table 2. Figures 9, 10, and 11 show the phase fractions for layer one at the end of the first, third and fifth scans. Here the layers were modelled, and the microstructure was taken immediately after the scan had ended. The rapid heating and elevated temperatures cause $\alpha$ to $\beta$ transformation to take place above the $\beta$ transus; on cooling $\beta$ to $\alpha$ transformation begins at $\beta$ transus temperature. Martensite transformation completes below the $T_{ms}$ temperature, where the $\beta$ to $\alpha'$ dominates. We will see the highest temperatures in layer one for the 1st scan. The figure shows that as the beam has moved along the scan line, the material has been fully melted, leaving the phase fraction as 100% $\beta$. The material melted at the end of the scan remained as $\alpha$, and no martensite phase was seen. With subsequent laser scans being made to layers above, the temperature in layer one has reduced; however, it is still large enough to cause a majority $\beta$ phase. At the start of the scan, it can be seen that martensite has started a transformation. By the time the 5th scan has passed, the martensite has continued to grow, with the highest fraction around 0.35. Adding layers will undoubtedly impact the lower layers, cooling slower and experiencing less time at high temperatures, transforming some of the $\beta$ into $\alpha$. Results from the 1st case simulation can be seen in Figs. 12 and 13 where a node on the end of the 1st layer has been selected for analysis. The temperature evolution is plotted over 2.75 seconds along with the liquidus, solidus, $\beta$ transus and martensite. $\alpha$, $\beta$ and martensite evolution are plotted over the same time scale and displayed below the temperature evolution. Martensite fraction has been designated yellow shading, $\beta$ red and $\alpha$ blue.

At the beginning of the simulation, the temperature rises above the solidus temperature, resulting in the 100% $\beta$ phase. Melting and solidification occur rapidly where thermal gradients grow above the necessary condition for martensite transformation of 410°C/s. The $\beta$ phase transforms into martensite at the martensite start temperature (575°C). As the second layer is melted, the temperature rises on the first layer past the beta transus temperature. Again, the martensite transformation begins. This process is repeated as further layers are scanned with the martensite temperature reaching equilibrium as 35%. An issue with modelling the $\alpha$ transformation causes it to be modelled incorrectly. As a new powder layer assigned an $\alpha$ state, it influences the layer below, causing a spike visible in Fig. 12 by the blue lines around the laser scans at 0.5-second intervals. Where the temperature is large enough to reach the $\beta$ transus, the $\alpha$ formation and dissolution can be analysed. The martensite calculated is typical of those in the characterisation of Ti6Al4V samples built by SLM. The model was repeated without accounting for re-coating to analyse how the 1st layer reacted to five scans and how the microstructure evolved along with each layer at the end of the fifth scan. By not considering the addition of further a re-coating time $\alpha$ formation could be seen. However, further work will be required to model the $\alpha$ dissolution with time allowed for re-coating and cooling.

In Fig. 13, layers 1, 3 and 5 are shown at the end of the fifth scan. Layer 1 at the end of scan 5 shows martensite, $\alpha$ and $\beta$, as discussed above. In layer 3, the area where the laser beam is directly above can provide a high percentage of the $\beta$ phase. Moving away from the beam, the phase transforms to $\alpha$ and martensite. On the top surface, martensite is more likely to experience higher cooling rates. The bottom layer experiences longer melt pools and more heating cycles. This reheating slows the martensite concentration down, which is why it is more significant in scan five than in scan 1. Martensite conditions are fulfilled in most of the process, so there is little alpha formation. Also, not much time has been allowed for cooling, so transformations have not been completed. From the abovementioned uncertainties, work is still required to validate the model and control for adding layers correctly.

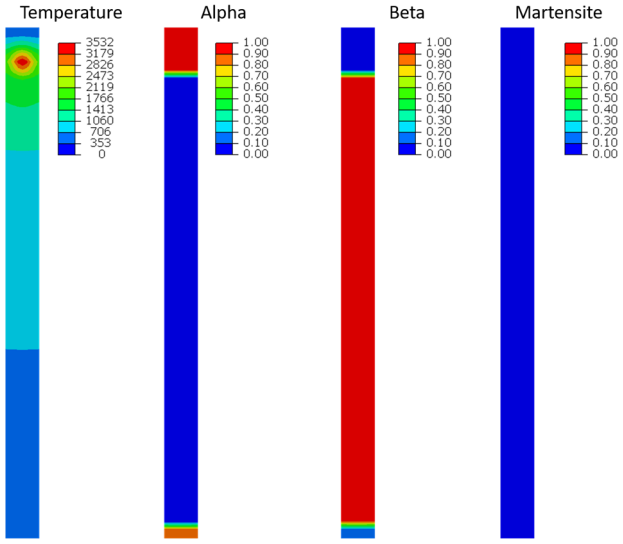


**Fig. 9.** Simulated phase fractions and temperature distribution for layer 1 at end of scans 1.

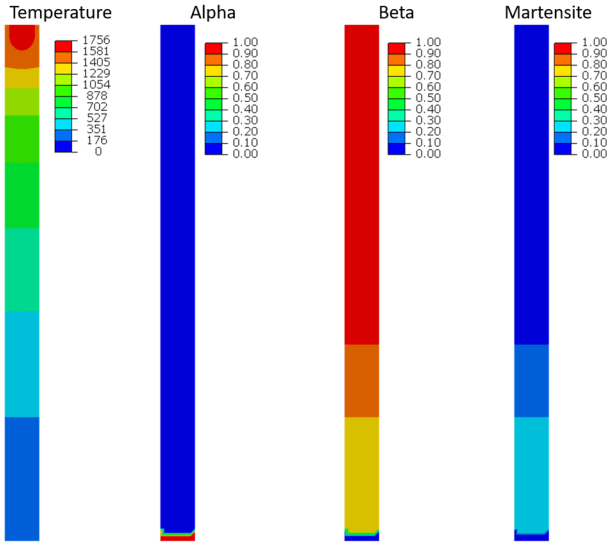


**Fig. 10.** Simulated phase fractions and temperature distribution for layer 1 at end of scans 3.

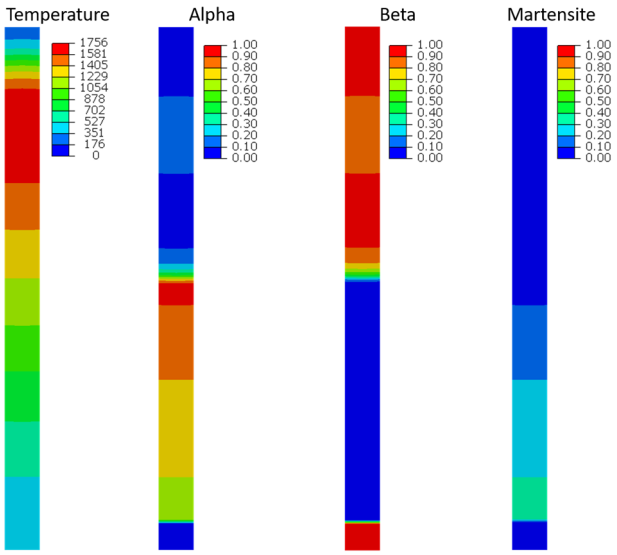


**Fig. 11.** Simulated phase fractions and temperature distribution for layer 1 at end of scans 5.

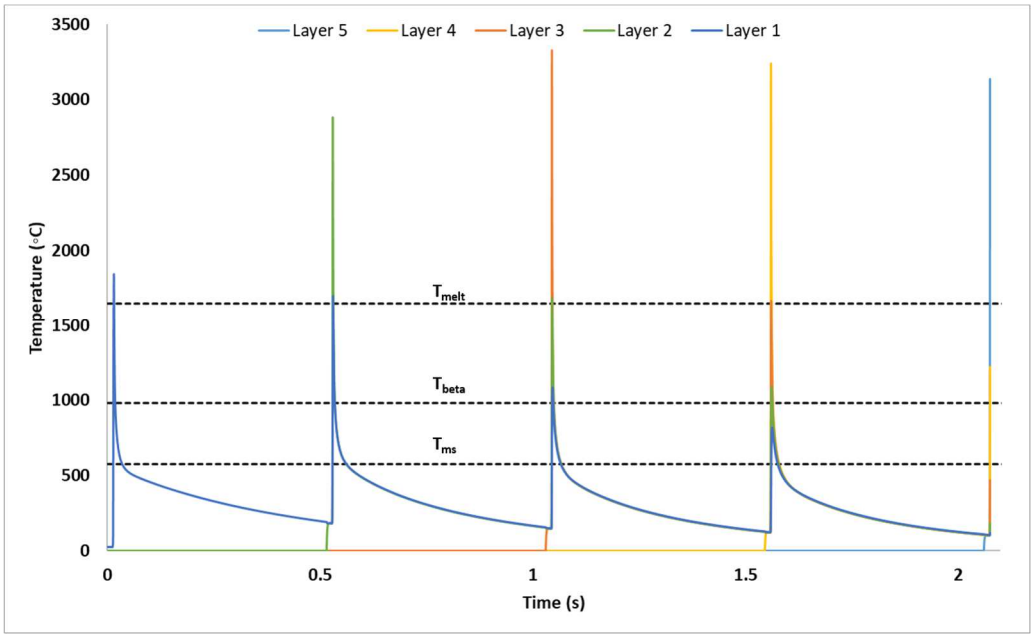


**Fig. 12.** Temperature evolution at the end point of scan 1 for layer 1 (Case 1).

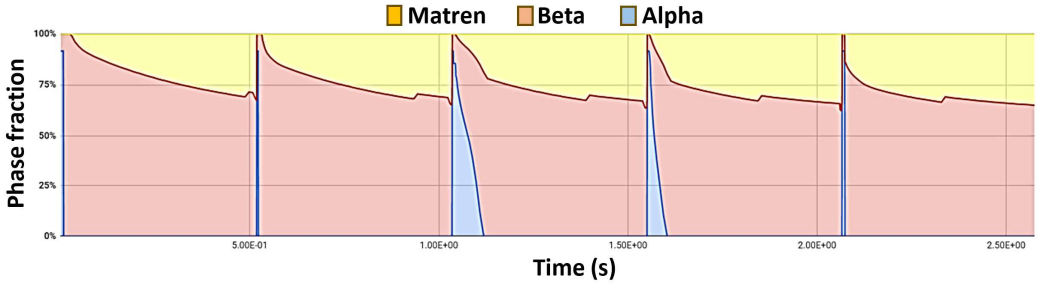


**Fig. 13.** Microstructure evolution at the end point of scan 1 for layer 1 (Case 1).

### 4.1. Processing Parameter Influence

The section aims to provide detailed insights into how variations in processing parameters, such as laser power and scanning speed, influence the microstructural evolution of Ti6Al4V during the Selective Laser Melting (SLM) process. This section is included towards the end of the paper to build upon the theoretical framework and model validation discussed earlier, ensuring that the reader has a comprehensive understanding of the foundational aspects before delving into specific applications and their implications.

The effect of two different processing conditions is considered in this section, as shown in Table 2. The first case (Case 2) examines the influence of increasing laser powers. The results of this investigation are illustrated in Figs. 14 and 15. Compared to the baseline 100 W test, it was observed that more significant temperatures are reached during each scan when higher laser powers are used. Specifically, the second scan provides enough energy to melt the first layer completely. Martensite transformation begins when the temperature falls below the martensite start temperature (TMS). However, a direct comparison of $\alpha$ formation was not feasible due to the re-coating issue. It was found that the final martensite fraction did not change significantly as it reached equilibrium. Nevertheless, a smoother transition is attributed to longer durations at elevated temperatures, which create lower cooling rates.

By increasing the temperature, only minor changes were observed in martensite formation. This indicates that further analysis is necessary to thoroughly understand $\alpha$ evolution once the re-coating issue has been resolved. The second case (Case 3) investigates the influence of increasing scanning velocities. The temperature evolution and phase evolutions for this case are shown in Figs. 16 and 17. Compared to the 100 W test, the results indicate much-reduced temperatures, as less time is allowed for the laser beam to transfer energy to the material. Despite these reduced temperatures, the martensite formation did not change significantly since the temperature for martensite formation (TMS) was still reached. Similar to the previous case, $\alpha$ formation could not be compared accurately due to the re-coating issue. Further analysis with a broader range of processing parameters is required to explore how the microstructure evolves under different conditions fully.

Including this section at the end of the paper serves several purposes. Firstly, it demonstrates the practical implications of the predictive model developed earlier in the study. The study can provide actionable recommendations for optimising SLM process parameters to achieve desired microstructural characteristics and mechanical properties by applying the model to different processing scenarios. Secondly, this placement ensures that the reader understands the model's validity and accuracy before considering its practical applications. This logical progression from theory and validation to application and optimisation helps maintain the clarity and coherence of the paper.

The figures accompanying this section illustrate the temperature evolution and microstructure changes for the different processing conditions. Figure 14 shows the temperature evolution at the end point of scan 1 for layer 1 in Case 2, while Fig. 15 depicts the microstructure evolution under the same conditions. Similarly, Fig. 16 presents the temperature evolution for Case 3, and Fig. 17 illustrates the corresponding microstructure evolution. These visual aids help clarify the effects of varying laser power and scanning speed on the SLM process, clearly comparing the resulting microstructures. It is crucial for understanding the practical implications of the predictive model and offers valuable insights into optimising SLM process parameters. By analysing different scenarios and their effects on microstructure evolution, the study provides a comprehensive approach to improving the efficiency and quality of additive manufacturing for critical aerospace, biomedical, and automotive applications.

The observed steep temperature drop in layer 1 during each scan, as depicted in the temperature evolution figures of Section 4.1, can be attributed to several key factors intrinsic to the Selective Laser Melting (SLM) process.

Firstly, the rapid heating and cooling cycles inherent to the SLM process play a significant role. The SLM process involves the rapid heating of the material as the laser scans over a specific area, followed by equally rapid cooling once the laser has passed. This results in steep temperature gradients within the material. When the laser moves away from a particular point, the heat source is abruptly removed, causing a rapid decrease in temperature and leading to a steep temperature drop immediately after each scan.

Secondly, the thermal conductivity and heat dissipation characteristics of Ti6Al4V contribute to this behaviour. Ti6Al4V has relatively high thermal conductivity, so heat is quickly conducted from the heated zone to the surrounding material. The substrate and surrounding previously deposited layers act as a heat sink, dissipating the heat from the newly melted layer. This rapid heat dissipation contributes to the steep temperature drop observed in layer 1.

The layer thickness and scan strategy used in the SLM process also influence the temperature evolution. The SLM process typically uses thin layers of powder (around 60 $\mu$m in this case). Thin layers heat up and cool down more quickly than thicker layers, contributing to the sharp temperature changes. The scanning strategy, including the laser power and scan speed, affects how quickly the temperature rises and falls. Rapid scanning speeds and high laser power can lead to rapid heating, followed by a swift temperature drop as the laser moves to the following scan line.

Moreover, the cooling that occurs between scans also affects the temperature evolution. There is often a brief period between consecutive scans where the material can cool. This cooling period, although short, can lead to significant temperature drops, especially in the uppermost layers like layer 1. The time taken to apply a new layer of powder (re-coating time) also contributes to the cooling of the previously scanned layer, leading to a further decrease in temperature.

Finally, heat accumulation and residual heat within the system over multiple scans also play a role. In the initial scans, there is less heat accumulation in the system, leading to a more pronounced temperature drop. As more layers are added, the substrate and lower layers become progressively warmer, which can reduce the steepness of the temperature drop in subsequent layers. Over multiple scans, the system approaches a thermal equilibrium where the temperature drops may become less steep as the underlying layers retain more residual heat.

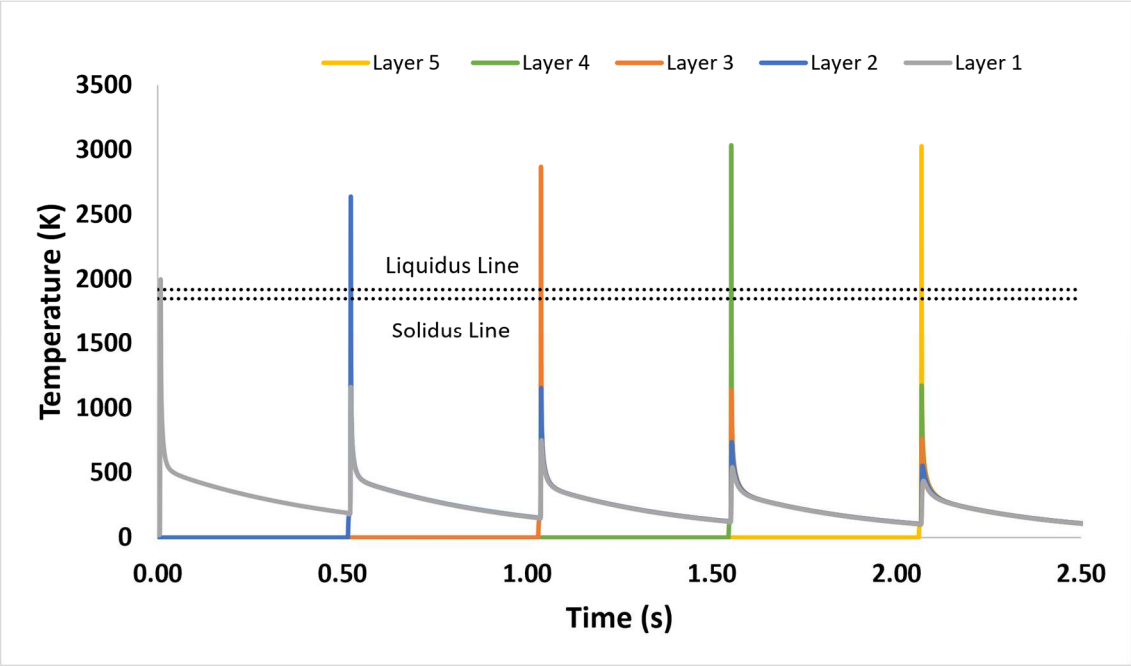


**Fig. 14.** Temperature evolution at the end point of scan 1 for layer 1 (Case 2).

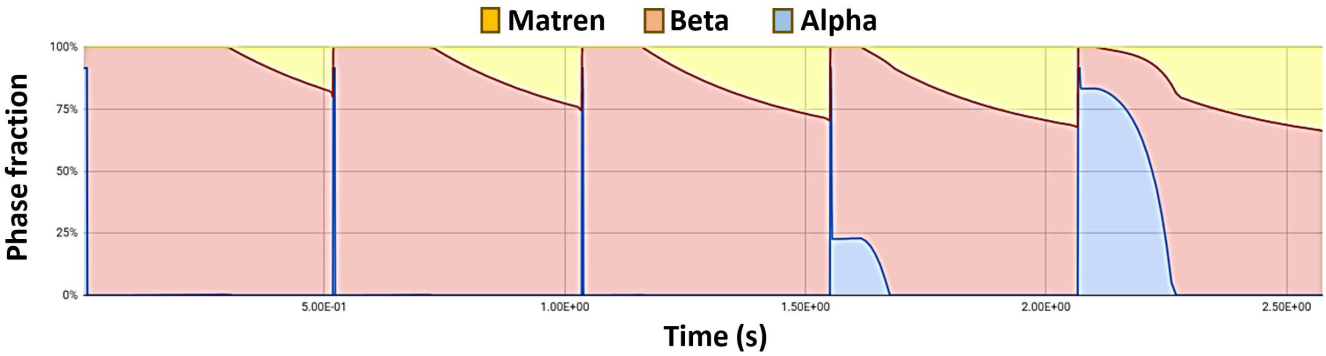


**Fig. 15.** Microstructure evolution at the end point of scan 1 for layer 1 (Case 2).

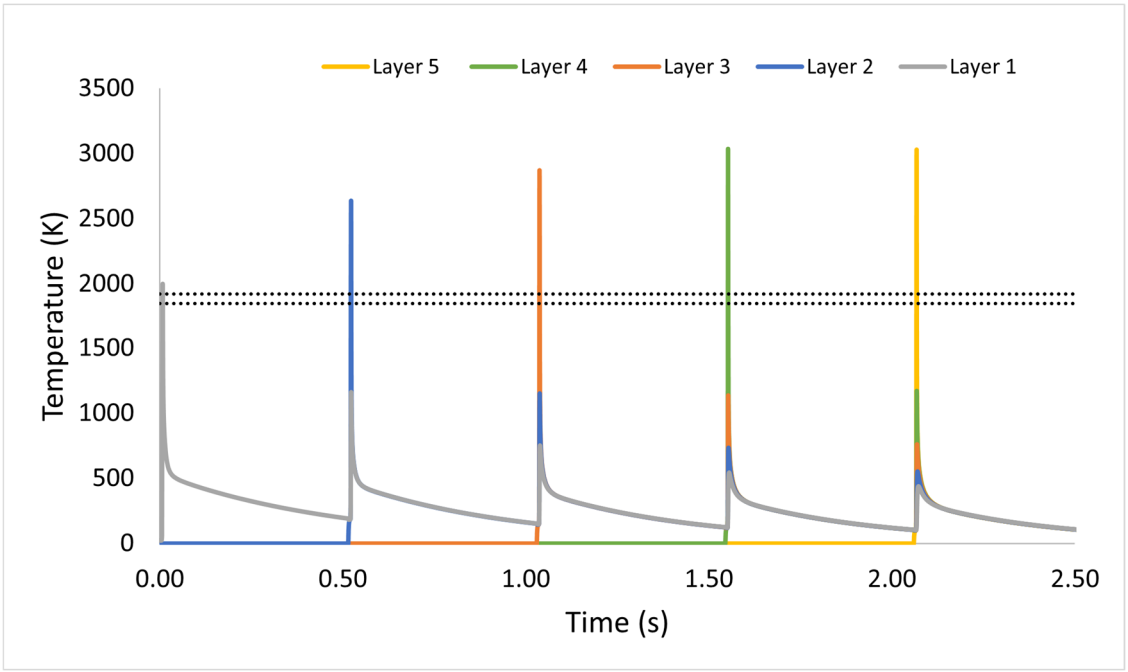


**Fig. 16.** Temperature evolution at the end point of scan 1 for layer 1 (Case 3).

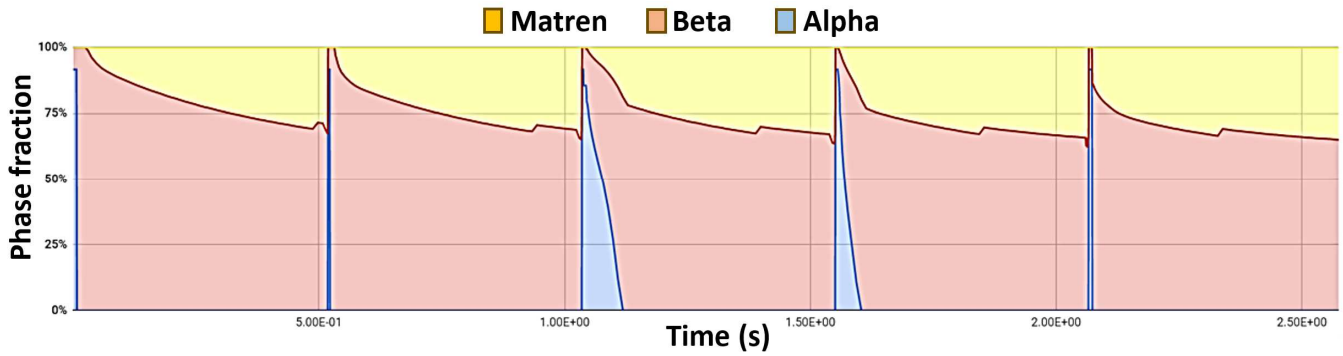


**Fig. 17.** Microstructure evolution at the end point of scan 1 for layer 1 (Case 3).

## 5. Conclusion

The developed microstructure evolution model for Ti6Al4V during the Selective Laser Melting (SLM) process offers significant advancements in predicting phase transformations and microstructural characteristics. By integrating thermal simulations with phase transformation kinetics, the model effectively predicts the formation and dissolution of alpha and martensite phases, providing a robust framework for optimising SLM parameters to achieve desired microstructural features.

**Key Insights:**

**Integration of Thermal and Microstructural Models:** The combination of Finite Element Analysis (FEA) for thermal history with the Johnson-Mehl-Avrami-Kolmogorov (JMAK) theory for phase transformations allows for accurate predictions of microstructure evolution. This integration is critical for understanding the SLM process's complex thermal cycles and phase kinetics.

**Impact of Processing Parameters:** The study highlights the significant influence of laser power and scanning speed on the microstructure. Higher laser powers and slower scanning speeds promote coarser microstructures, while faster cooling rates result in finer grains and higher martensite fractions. This understanding enables better control over the mechanical properties of the fabricated parts.

**Validation and Accuracy:** The model agrees well with experimental data, particularly in predicting alpha and martensite fractions under different cooling rates. The validation against differential scanning calorimetry (DSC) and resistivity measurements confirms the model's reliability.

**Challenges and Future Work:** Despite the advancements, the model's sensitivity to input parameters and the complexity of accurately capturing high thermal gradients and dynamic behaviour during SLM remain challenges. Future research should focus on refining the JMAK parameters, improving the representation of temperature-dependent transformations, and exploring broader ranges of processing parameters.

**Applications and Implications:** This comprehensive modelling approach reduces the reliance on trial-and-error methods, enhancing the efficiency and quality of additive manufacturing for critical applications in aerospace, biomedical, and automotive industries. The model is a valuable tool for guiding the design and optimisation of SLM processes, ultimately contributing to the broader field of additive manufacturing and material science.

In conclusion, the developed model provides significant insights into the microstructural evolution of Ti6Al4V during SLM, offering a pathway to optimise process parameters and improve the mechanical performance of manufactured parts. This work represents a step forward in predictive modelling for additive manufacturing, paving the way for more efficient and accurate production techniques in high-demand industries.

## Author Contributions

G. Abdelal, D. Higgin, C.W. Chan and B. Falzon planned the scheme, initiated the project, and suggested the experiments; D. Higgin and C.W. Chan conducted the experiments and analysed the empirical results; G. Abdelal and D. Higgin developed the mathematical modelling and examined the theory validation. The manuscript was written through the contribution of all authors. All authors discussed the results, and reviewed, and approved the final version of the manuscript.

## Acknowledgments

Not applicable.

## Conflict of Interest

The authors declared no potential conflicts of interest concerning the research, authorship, and publication of this article.

## Funding

The authors received no financial support for the research, authorship, and publication of this article.

## Data Availability Statements

The datasets generated and/or analysed during the current study are available from the corresponding author on reasonable request.

## Nomenclature

| | | | |
|---|---|---|---|
| SLM | Selective Laser Melting | $k$ and $n$ | Reaction rate constant and Avrami constant, respectively |
| Ti6Al4V | Titanium alloy composed of 6% Aluminum and 4% Vanadium | $X(t)$ | Transformed fraction at time $t$ |
| AM | Additive Manufacturing | $X_{eq}$ | Equilibrium fraction of a phase |
| JMAK Theory | Johnson-Mehl-Avrami-Kolmogorov Theory | $X_0$ | Initial fraction of a phase |
| FEA | Finite Element Analysis | $\tau$ | Equivalent time accounting for changes in temperature |
| DSC | Differential Scanning Calorimetry | $\gamma$ | Koistinen-Marburger constant |
| TTT Diagrams | Time-Temperature-Transformation Diagrams | $\alpha_{mdis}^{eq}(T)$ | Maximum dissolvable martensite at equilibrium at temperature $T$ |
| $\alpha$ Phase | One of the solid phases in the Ti6Al4V alloy, stable at lower temperatures | $k_m$ and $n_m$ | JMAK parameters for martensite dissolution |
| $\beta$ Phase | Another solid phase in the Ti6Al4V alloy, stable at higher temperatures | $F_{diss}(T)$ | Temperature-dependent function for phase dissolution |
| Martensite | A hard, brittle phase formed by rapid cooling | | |
| $\alpha'$ | Martensitic phase formed in Ti6Al4V during rapid cooling | | |
| $M_s$ Temperature | Martensite start temperature | | |
| $T_{ms}$ Temperature | Temperature at which martensite transformation starts | | |
| $\beta$ Transus Temperature | The temperature above which the $\beta$ phase is stable | | |

## References

[1] Khairallah, S.A., et al., Laser powder-bed fusion additive manufacturing: Physics of complex melt flow and formation mechanisms of pores, spatter, and denudation zones, *Acta Materialia*, 108, 2016, 36–45.
[2] Wang, X.C., et al., Direct selective laser sintering of hard metal powders: experimental study and simulation, *The International Journal of Advanced Manufacturing Technology*, 19(5), 2002, 351–357.
[3] Yang, Z., et al., Modeling laser beam absorption of metal alloys at high temperatures for selective laser melting, *Advanced Engineering Materials*, 23(9), 2021, 2100137.
[4] German, R.M., A quantitative theory for supersolidus liquid phase sintering, *Powder Metallurgy*, 34(2), 1991, 101–107.
[5] Ladani, L., et al., Effective liquid conductivity for improved simulation of thermal transport in laser beam melting powder bed technology, *Additive Manufacturing*, 14, 2017, 13–23.
[6] Gusarov, A.V., et al., Heat transfer modelling and stability analysis of selective laser melting, *Applied Surface Science*, 254(4), 2007, 975–979.
[7] Rosenthal, D., Mathematical theory of heat distribution during welding and cutting, *Welding Journal*, 20, 1941, 220–234.
[8] Nunes, A.C., An extended Rosenthal weld model, *Welding Journal*, 62(6), 1983, 165s–170s.
[9] Dai, K., Shaw, L., Thermal and mechanical finite element modeling of laser forming from metal and ceramic powders, *Acta Materialia*, 52(1), 2004, 69–80.
[10] Goldak, J., et al., A new finite element model for welding heat sources, *Metallurgical Transactions B*, 15(2), 1984, 299–305.
[11] King, W., et al., Overview of modelling and simulation of metal powder bed fusion process at Lawrence Livermore National Laboratory, *Materials Science and Technology*, 31(8), 2015, 957–968.
[12] Wang, L., *Particle scale modelling of powder spreading in powder bed fusion additive manufacturing*, PhD Thesis, Monash University, 2020.
[13] Weber, S., et al., Parameters on support structure design for metal additive manufacturing, *Proceedings of the Design Society: DESIGN Conference*, Vol. 1, Cambridge University Press, 2020.
[14] Sing, S.L., et al., 3D printing of metals in rapid prototyping of biomaterials: Techniques in additive manufacturing, *Rapid Prototyping of Biomaterials*, Second Edition, Woodhead Publishing Series in Biomaterials, Woodhead Publishing, 2020.
[15] Kruth, J.-P., et al., Binding mechanisms in selective laser sintering and selective laser melting, *Rapid Prototyping Journal*, 11(1), 2005, 26-36.
[16] Scheil, E., Anlaufzeit der Austenitumwandlung, *Archiv fur das Eisenhuttenwesen*, 8(12), 1935, 565–567.
[17] Koistinen, D.P., Marburger, R.E., A general equation prescribing the extent of the austenite-martensite transformation in pure iron-carbon alloys and plain carbon steels, *Acta Metallurgica*, 7(1), 1959, 59–60.
[18] Geijselaers, H.J.M., Numerical simulation of stresses due to solid state transformations: the simulation of laser hardening, PhD Thesis, University of Twente, 2003.
[19] Baykasoglu, C., et al., A process-microstructure finite element simulation framework for predicting phase transformations and microhardness for directed energy deposition of Ti6Al4V, *Additive Manufacturing*, 35, 2020, 101252.
[20] Sun, W., et al., A simulation and experiment study on phase transformations of Ti-6Al-4V in wire laser additive manufacturing, *Materials & Design*, 207, 2021, 109843.
[21] Kelly, S.M., *Thermal and microstructure modeling of metal deposition processes with application to titanium aluminum vanadium*, PhD Thesis, Virginia Polytechnic Institute and State University, 2004.
[22] Higgins, D., *Investigating the microstructure evolution of additive manufactured parts using multiscale modelling*, PhD Thesis, Queen's University of Belfast, Northern Ireland, UK, 2023.
[23] Malinov, S., et al., Differential scanning calorimetry study and computer modelling of β→α phase transformation in a Ti-6Al-4V alloy, *Metallurgical and Materials Transactions A*, 32(4), 2001, 879–887.
[24] Malinov, S., et al., Resistivity study and computer modelling of the isothermal transformation kinetics of Ti–6Al–4V and Ti–6Al–2Sn–4Zr–2Mo–0.08 Si alloys, *Journal of Alloys and Compounds*, 314(1-2), 2001, 181–192.
[25] Babu, S.S., et al., Measurement of Phase Transformation Kinetics During Repeated Thermal Cycling of Ti-6Al-4V Using Time-Resolved X-Ray Diffraction, URL: https://www.osti.gov/biblio/1008995.
[26] Murgau, C.C., Pederson, R., Lindgren, L.E., A model for Ti–6Al–4V microstructure evolution for arbitrary temperature changes, *Modelling and Simulation in Materials Science and Engineering*, 20(5), 2012, 055006.

## ORCID iD

Gasser Abdelal https://orcid.org/0000-0002-9850-1633
Chi-Wai Chan https://orcid.org/0000-0003-4953-1024
Brian Falzon https://orcid.org/0000-0002-3613-2924



**How to cite this article:** Abdelal G., Higgins D., Chan C.W., Falzon B. Insights into Phase Transformations during Selective Laser Melting of Ti6Al4V: A Numerical Approach, *J. Appl. Comput. Mech.*, 11(2), 2025, 399-415. https://doi.org/10.22055/jacm.2024.47217.4677